



A flexible z-coordinate approach for the accurate representation of free surface flows in a coastal ocean model (SHYFEM v. 7_5_71)

Luca Arpaia¹, Christian Ferrarin¹, Marco Bajo¹, and Georg Umgiesser^{1,2}

¹Institute of Marine Sciences, National Research Council, Castello 2737/F, 30122 Venice, Italy

²Klaipėda University, Coastal Research and Planning Institute, H.Manto 84, 92294 Klaipėda, Lithuania

Correspondence: Luca Arpaia (luca.arpaia@ve.ismar.cnr.it)

Abstract. We propose a z-coordinate algorithm for ocean models which, thanks to the insertion and removal of surface layers, can deal with an arbitrarily large tidal oscillation independently of the vertical resolution. The algorithm is based on a classical two steps procedure used in numerical simulations with moving boundaries (grid movement followed by a grid topology change, that is insertion/removal of surface layers) which leads to a stable and accurate numerical discretization. With ad-hoc treatment of advection terms at non-conformal edges that may appear due to insertion/removal operations, mass conservation and tracer constancy are preserved. This algorithm, called z-surface-adaptive, can be reverted, in particular case when all layers are moving, to other z-surface-following coordinates, such as z-star or quasi-z. With simple analysis and realistic numerical experiments, we compare the surface-adaptive-z coordinate against z-star and we show that it can be used to simulate effectively coastal flows with wetting and drying.

10 1 Introduction


The accuracy of ocean models in reproducing many dynamical processes is highly related to their vertical coordinate system. In literature, many choices exist covering the spectrum of coordinate systems. There are four main types of vertical coordinates: 1) isopycnal coordinates with the interfaces that follow the materials (Lagrangian framework); 2) z-coordinates with fixed interfaces parallel to geo-potentials (Eulerian framework); 3) terrain/surface-following sigma or S-coordinates with interfaces adapted to the ocean surface and bottom boundaries; 4) adaptive coordinate with interfaces that dynamically adapt to better capture different flow features (Lagrangian tendencies, stratification and shear). The last two coordinates move "arbitrarily" with respect to the flow, either to adapt to the free surface or any other features, and belong to the Arbitrary Lagrangian Eulerian framework (ALE).

Z-coordinates were used in early ocean models. Such discretization based on fixed interfaces has issues with the complex and moving boundaries represented by the free surface and by the ocean bottom. Despite this disadvantage, z-coordinate are still implemented and used in some ocean models (HAMSOM, Backhaus, 1985), (TRIM-3D, Cheng et al., 1993), (SHYFEM, Umgiesser, 2022) and they are attractive when simulating stratified flows as in Hordoir et al. (2015). This occurs because the z-interfaces are well aligned to isopycnals and the internal pressure gradient term does not suffer from pressure gradient error.




To simplify the boundary condition at the free surface, z -coordinates were typically coded allowing the surface layer to vary
25 in thickness (Griffies et al., 2001). However, in such models, the surface layer cannot vanish, which implies that the free surface
variation must be smaller than the surface layer thickness. For coastal applications, this is a serious drawback, especially for the
vertical resolution in shallow areas with high tidal elevations. In order to overcome this problem, other z -type coordinates have
been introduced over the years. These vertical coordinates use the ALE transformation to accommodate the tidal oscillation,
but the bottom is not a coordinate surface (they are surface-following but not terrain-following). These coordinates are clearly
30 of ALE-type but in the ocean modelling literature they are classified as z because the deviation from the geo-potentials is very
small. They combine small diapycnal mixing and small pressure gradient errors. The z -star of Adcroft and Campin (2004),
the *quasi- z* of Mellor et al. (2002) and the *hybrid z 's* of Burchard and Petersen (1997) all belong to such *z -surface-following*
system, see Figure 1. An alternative to deal with the moving surface is to keep the grid perfectly aligned to geo-potentials, thus
working in a truly Eulerian framework, but allowing the surface layer(s) to be removed or inserted. We refer to this system as z -
35 *surface-adaptive*. Insertion/removal of the top layer has been discussed in Casulli and Cheng (1992) and it is used for example
in Burchard and Baumert (1998). However "both the accuracy and stability are suspect; it is most likely difficult to make the
transition of a vanishing layer smooth enough to not generate numerical problems; conservation issues are a major concern and
the likelihood of vanishing layers become more frequent with increasing vertical resolution" (Adcroft and Campin, 2004).

In this manuscript, we review z -coordinate performances relative to the treatment of the free surface boundary. We propose a
40 solution to the stability and conservation issues for the insertion/removal. We employ a classical grid adaptation strategy when
the adaptation is driven by a moving boundary (Guardone et al., 2011). It combines a first ALE grid movement step (surface
interface displacement stretched by the free surface displacement) and a second topology modification step (layer insertion,
layer removal). All these operations are easily performed on the one-dimensional vertical grid. We show that this solution
generalizes z -coordinates in the sense that the same algorithm can be easily reverted to z -surface-following coordinates and
45 can be added to a flexible vertical coordinate system. In fact, the grid adaptation has one free parameter that controls the number
of moving layers. Tuning such parameter, so that all the layers along the water column are moving, we show the link of the
proposed approach with the z -surface-following coordinates.

Finally, we look at a second potential drawback  using fixed interfaces with a free surface. The large vertical veloc-
ity triggered by the free surface oscillation can cause strong numerical mixing with respect to the surface-following coordi-
50 nates (Klingbeil et al., 2018). We quantify such additional spurious mixing of z -coordinates theoretically and numerically and
we highlight the dependencies from the external forcing (tidal characteristics, stratification profile) and the numerics (vertical
advection scheme, vertical grid size).

The algorithm is implemented in the SHYFEM finite-element ocean model of the CNR-ISMAR (Umgiesser et al. (2004),
<https://github.com/SHYFEM-model/shyfem>) which uses a popular choice for many coastal ocean models influenced by the
55 work of Backhaus (1983), that is a semi-implicit finite element discretization on unstructured B-type grids.

The manuscript is organized as follows: in Section 2 we introduce the vertical discretization, the layerwise  Shallow Water
equations, and we discuss the spurious mixing effect caused by a barotropic tide. In Section 3 we describe the z -surface-adaptive

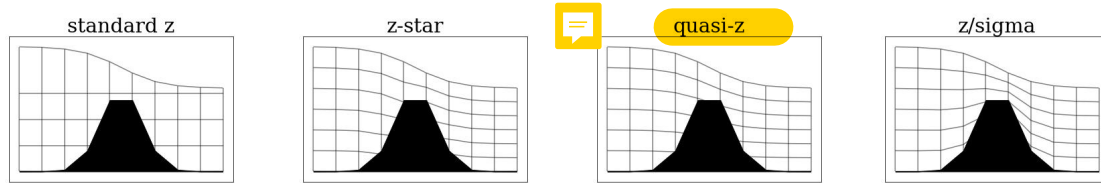


Figure 1. One dimensional sketch of different vertical z-grids existing in the literature. From left to right: standard z with fewer layers due to the limitation for the surface layer thickness, z-star, quasi-z, hybrid z/sigma

algorithm, in Section 4 we detail the issue of a spatially variable number of surface layers caused by the insertion/removal operations. In Section 5 we provide numerical tests and in Section 6 we conclude with a discussion.

60 2 Layerwise Shallow Water model with z-coordinate

We consider the layerwise (or layer integrated) shallow water model for stratified flows discussed in Burchard and Petersen (1997) and studied in Audusse et al. (2011b), Audusse et al. (2011a). We use the one-dimensional case to present the main concepts. The layerwise shallow water model is based on a discretization of the water column with a vertical grid composed of N layers denoted by greek letters and ordered from the free surface $\zeta(x, t)$ ($\alpha = 1$) to the bottom $b(x)$ ($\alpha = N$). Each layer α is delimited by the interfaces $z_{\alpha\pm 1/2}$. The surface and bottom interfaces are respectively $z_{1/2} = \zeta$ and $z_{N+1/2} = -b$. Standard z-coordinate models with fixed interfaces have been enhanced over time to deal with the oscillation of the free surface. Typically a vertical moving grid is introduced, defined by a surface-following transformation from a reference fixed space with coordinate $s \in [0, -z_b(x)]$ to the physical space with vertical coordinate $z \in [\zeta, -b(x)]$:

$$z = z(x, s, t) = \zeta(x, t) + f(x, s, t) \quad (1)$$

with $f(x, s, t) = S(s)(z_b(x) + \zeta(x, t))$. Among the coordinates that have been proposed to enhance geo-potentials we mention:

- 70 – the z-star coordinate (Adcroft and Campin, 2004) $z_b = b(x) \rightarrow s = \frac{z}{z_b}$ with stretching function $S = \frac{z^*}{b(x)}$;
- the quasi-z coordinate (Mellor et al., 2002) $z_b = \max b(x) \rightarrow s = \frac{z - z_b}{z_b - z_b}$ with stretching function $S = \frac{z^{qz}}{\max b(x)}$;
- the hybrid z/sigma (Burchard and Petersen, 1997): $z_b = b(x)$ since the transformation is linear in S , a blend between the z-star and the sigma coordinate $\sigma \in [0, -1]$ through a parameter θ is possible. The stretching function is $S = \frac{z^*}{b(x)}\theta + \sigma(1 - \theta)$.

75 Standard z-coordinate is a particular case where coordinate lines do not depend on time and space. Of course, this is implemented by allowing the top layer to vary in thickness without vanishing (Griffies et al., 2001), see Figure 1 for an illustrative example of these different z-grids. To account for the domain movement, the layerwise equations are written in a moving frame and, hereinafter, all partial derivatives ∂_a are not the standard Eulerian ones but they have to be intended in the moving



80 frame (the so-called ALE derivatives (Hirt et al., 1974)): horizontal derivatives are taken along constant s -line $\partial_x = \partial_x|_s$ while temporal derivatives are measured from an observer moving with the grid $\partial_t = \partial_t|_s$. Please note the difference between the ALE time derivative and the Lagrangian time derivative of the position:

$$\sigma_{\alpha+1/2} = \frac{\partial z_{\alpha+1/2}}{\partial t} \quad w_{\alpha+1/2} = \frac{dz_{\alpha+1/2}}{dt}$$

with σ the velocity of the grid interface and w the vertical fluid velocity at $z_{\alpha+1/2}$. For each layer we define the layer thickness:

$$h_\alpha = z_{\alpha-1/2} - z_{\alpha+1/2}$$

The layerwise model is based on a piecewise constant approximation of the horizontal velocity on the vertical grid. The layer average is:

$$u_\alpha = \frac{1}{h_\alpha} \int_{z_{\alpha+1/2}}^{z_{\alpha-1/2}} u dz \quad (2)$$

85 Then the layerwise shallow water model reads:

$$\frac{\partial \zeta}{\partial t} + \frac{\partial}{\partial x} \left(\sum_{\alpha=N}^1 h u_\alpha \right) = 0 \quad (3)$$

$$\frac{\partial h u_\alpha}{\partial t} + \frac{\partial h u_\alpha u_\alpha}{\partial x} = [uG]_{\alpha+1/2}^{\alpha-1/2} - g h_\alpha \frac{\partial \zeta}{\partial x} + IPG_\alpha + \left[\nu_v \frac{\partial u}{\partial z} \right]_{\alpha+1/2}^{\alpha-1/2} \quad (4)$$

As is customary, the mass equation is integrated over the whole water column. IPG_α is the internal pressure gradient force written in the density Jacobian form of Song (1998) and based on a piecewise constant approximation of the density ρ_α as in (2). ν_v is the vertical viscosity and the vertical derivative in the diffusion term is resolved with finite differences. The definition of the mass-transfer function $G_{\alpha\pm 1/2}$ responsible for the exchange between the layers is:

$$G_{\alpha-1/2} = \left(\frac{\partial z}{\partial x} \Big|_{\alpha-1/2} u_{\alpha-1/2} \right) + \sigma_{\alpha-1/2} - w_{\alpha-1/2} \quad (5)$$

which is typically computed by summing the layerwise mass equation:

$$G_{\alpha-1/2} = G_{\alpha+1/2} + \frac{\partial h_\alpha}{\partial t} + \frac{\partial h u_\alpha}{\partial x} \quad (6)$$

from the bottom layer N to layer α with $G_{N+1/2}$ that accounts for the bottom boundary condition and $G_{1/2} = 0$ that ensures vertical mass conservation. At the end we solve for $N + 1$ unknowns, namely the free surface level ζ and N momentum fluxes $h u_\alpha$ $\alpha = 1, N$.

95 We assume that the fluid density depends on a given set of tracers through an equation of state of type $\rho(T, S)$ where $T(x, t)$ is the temperature and $S(x, t)$ is the salinity. Each tracer is governed by an advection-diffusion equation:

$$\frac{\partial h t_\alpha}{\partial t} + \frac{\partial h t_\alpha u_\alpha}{\partial x} = [tG]_{\alpha+1/2}^{\alpha-1/2} + \left[\nu_{tv} \frac{\partial t_\alpha}{\partial z} \right]_{\alpha+1/2}^{\alpha-1/2} \quad (7)$$



where ν_{tv} is the vertical tracer diffusivity. This advection diffusion equation admits a trivial solution which we want to inherit also at the discrete level, the so-called tracer **constancy** condition. In fact, for constant tracer $t_\alpha = \text{const}$, equation (7) reduces to layerwise mass equation (6). This is also called the Geometric Conservation Laws (GCL) condition in ALE compressible flow simulations.

For a standard z -layer model, the interfaces do not depend on **location** or time, except for the free surface interface. In (5), or equivalently in (6) using a layerwise integration of the incompressibility $[w]_{\alpha+1/2}^{\alpha-1/2} = -h_\alpha \frac{\partial u_\alpha}{\partial x}$, if the depth of layers does not change in time, the mass-transfer function coincides with the vertical velocity:

$$\left. \frac{\partial z}{\partial x} \right|_{\alpha-1/2} = 0, \quad \sigma_{\alpha-1/2} = 0 \quad \rightarrow \quad G_{\alpha-1/2} = -w_{\alpha-1/2}, \quad \alpha = 2, N+1$$

To complete (4) and (7) we have to give the expressions for the prognostic variables at the top/bottom interfaces. Consistently with the Finite Volume vertical discretization, the tracer and the horizontal velocity at the interface are computed with a numerical flux. The majority of ocean models, including SHYFEM, use a Total Variation Diminishing (TVD) flux. For the tracer, the TVD flux reads (LeVeque, 2002):

$$G_{\alpha-1/2} t_{\alpha-1/2} = G_{\alpha-1/2}^+ t_\alpha + G_{\alpha-1/2}^- t_{\alpha-1} + \frac{|G_{\alpha-1/2}|}{2} \left(1 - \left| \frac{G_{\alpha-1/2} \Delta t}{\Delta z_{\alpha-1/2}} \right| \right) (t_\alpha - t_{\alpha-1}) \phi \quad (8)$$

with $G^+ = \max(0, G)$, $G^- = \min(0, G)$, $\Delta z_{\alpha-1/2} = \frac{h_\alpha + h_{\alpha-1}}{2}$ and Δt the time step. Here we consider the Superbee flux limiter ϕ which is close to one in smooth regions (second-order accurate Lax-Wendroff flux) while it is close to zero in presence of large vertical gradients (first-order accurate upwind flux).

With a local truncation error analysis, we can further analyze the error typically associated with the vertical z -coordinate discretization when large vertical velocities induced by the tidal flow are present. Under the hypothesis of a passive tracer advected by a linearized barotropic tidal flow, we have computed the following upper bound for the vertical numerical diffusion induced by the oscillation of the water level:

$$D_\alpha^{num} \leq \frac{1 - \phi_\alpha}{2} A \Omega \left. \frac{\partial^2 t}{\partial z^2} \right|_\alpha h + \frac{1}{6} \frac{A \Omega}{H_0} \left. \frac{\partial^2 t}{\partial z^2} \right|_\alpha h^2 + O(h^3) \quad (9)$$

where h the uniform vertical grid-spacing, A the tidal amplitude, $\Omega = 2\pi/T$, T the tidal period and H_0 is the bottom depth. Unsurprisingly, the leading order term is a first-order upwind diffusion with a coefficient that depends on the tidal amplitude and is tuned by the limiter. For a smooth, profile this term is zero ($\phi \approx 1$) or even of anti-diffusive nature ($\phi > 1$), while for a non-smooth profile ($\phi \approx 0$) this term dominates. Interestingly there is also a second-order term that comes from the linear advection velocity, with a coefficient that depends on the non-linear parameter of the tidal wave A/H_0 . This can also be large for shallow depths. The numerical diffusion should be always compared to the physical diffusion $D_\alpha^{phy} = \nu_{tv} \partial_{zz} t$. The magnitude of each contribution depends on the tracer vertical profile as well as on the tidal parameter and the bottom depth. In the Appendix, we give the details of the formula (9) and we compute it for some idealized situations. We also confirm numerically the results. Both the theoretical and numerical results suggest that, for micro-tidal applications and typical vertical resolution of coastal models, the additional numerical error of z -coordinate is negligible while for higher tidal amplitude/coarser resolution the use of z -coordinate should be discouraged.

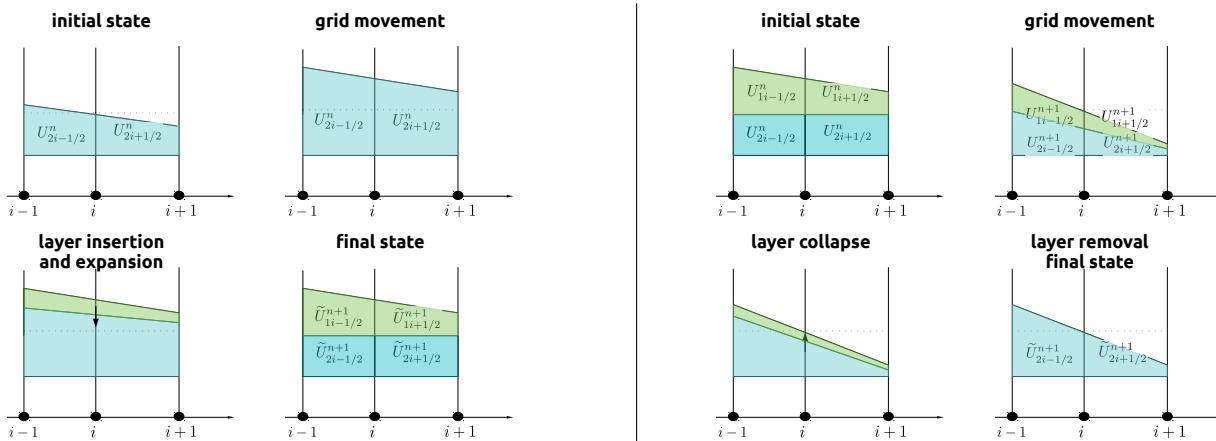


Figure 2. Grid and solution evolution during one time step. The process is interpreted as four stages which bring from the pair (U_h^n, ζ_h^n) to $(\tilde{U}_h^{n+1}, \zeta_h^{n+1})$. The vector $U = \{u_1, u_2\}$ collects the layer values of a generic layerwise scalar variable. Dashed line means removed interface. Left: case of top layer insertion. Right: case of top layer removal.

3 z-surface-adaptive coordinate

In this section, we detail the algorithm for the novel z-surface-adaptive coordinates. It is based on two steps: a first vertical *grid movement* step (interface displacement) and a second *topology modification* step (layer insertion, layer removal). The solution is interpolated across the grids: 1) for the grid movement, we have already written the layerwise equations in a moving frame, thus we compute the solution directly onto the new deformed grid; 2) for the grid topology change, we use conservative remaps. Both operations are described in the following paragraphs.

We consider numerical schemes for the layerwise Shallow Water equations that work with a discretization of the computational domain $[0, L]$ composed by a sequence of non-overlapping intervals or elements E , each with length Δx_E . The nodes of the horizontal grid are placed at $x_i = \sum_{E=1}^{i-1} \Delta x_E$, $i = 1, M + 1$. The element sharing node i and $i + 1$ is also denoted as $E = i + 1/2$. For example, the median dual cell obtained by joining the barycenters of the elements joining in i , $C_i = \frac{1}{2} (\Delta x_{i-1/2} + \Delta x_{i+1/2})$. On such horizontal grid, we denote the space discrete variables as $u(x) \approx u_h(x)$ and we identify approximation of variables at nodes as $u_i = u_h(x_i)$ and at elements as $u_{i+1/2} = u_h(x_{i+1/2})$. In a Finite Volume context the pointwise notation stands for the averaged values. We suppose that the numerical scheme computes the variables at the discrete time instants $t^n = t^0 + n\Delta t$ with time step Δt . We note by $u_h^n(x) = u_h(x, t^n)$ the fully discrete variable, that is the value of u_h at time t^n .

On the vertical, layers are contained in the set $\alpha = \{1, 2, \dots, N\}$. For a z-grid the number of layers varies with x and it is defined locally, e.g. at nodes $\alpha_i = \{1, 2, \dots, N_i\}$ and at elements $\alpha_E = \{1, 2, \dots, N_E\}$. We denote each layer interface at rest as $z_{\alpha \pm 1/2}^0$ and each layer thickness at rest as Δz_{α}^0 . After both the horizontal and the vertical z-coordinate discretizations, the domain is subdivided into quadrilateral boxes $E \times [z_{\alpha+1/2}, z_{\alpha-1/2}]$. At the bottom, z-coordinate models apply a mask to non-existing boxes that make the grid stepped.



3.1 Vertical grid movement

We restrict either to explicit or to semi-implicit time marching schemes that update the free surface from the discrete version of (3). Once ζ_h^{n+1} is available (without loss of generality, we assume that the free surface is updated at nodes ζ_i^{n+1}), we move the surface layers with the following steps:

- 150 – Identification of the layers spanned by free surface, through the set of indexes:

$$\alpha_{mov,i} = \left\{ \alpha : z_{\alpha-1/2}^0 + \epsilon_{mov} > \zeta_i^{n+1} \right\} \quad (10)$$

ϵ_{mov} is a small and positive constant that fixes the minimum allowable depth for a layer. Below this threshold, the vertical grid movement is deployed. ϵ_{mov} can be used to control the number of moving layers. The number of layers contained in the set is $N_{mov,i}$ and the upper-most and bottom-most layers are denoted respectively by $\alpha_{movTop,i} = \min \alpha_{mov,i}$ and $\alpha_{movBot,i} = \max \alpha_{mov,i}$. The depth of the moving layers is:

$$b_{mov,i} = \max(z_{\alpha_{movBot,i}+1/2}, -b_i)$$

- 155 – Computation of the new depth after a local grid deformation that absorbs the free surface movement. We use the generalized coordinates (1) which, at a discrete level, takes the form:

$$z_{\alpha+1/2,i}^{n+1} = \zeta_i^{n+1} + S_{\alpha+1/2,i} (\zeta_i^{n+1} + b_{mov,i}) \quad (11)$$

this time with S -function $S_{\alpha+1/2}$ such that $S_{\alpha+1/2} = 0$ for $\alpha+1/2 = \zeta_i$ and $S_{\alpha+1/2} = -1 \rightarrow z_{\alpha+1/2} = b_{mov,i}$. With $S_{\alpha+1/2,i} = -\sum_{\beta=\alpha_{top,i}}^{\alpha} l_{\beta,i}$, the nodal layer thickness reads:

$$h_{\alpha,i}^{n+1} = l_{\alpha,i} (\zeta_i^{n+1} + b_{mov,i}), \quad \alpha \in \alpha_{mov,i} \quad (12)$$

For the proportionality coefficients, we have used a z -star definition $l_{\alpha,i} = \frac{\Delta z_{\alpha}^0}{b_{mov,i}}$, see Section (2).

- 160 After the prognostic variables update on the moving grid, i.e. momentum $hu_{\alpha,h}^n \rightarrow hu_{\alpha,h}^{n+1}$ and tracers $t_{\alpha,h}^n \rightarrow t_{\alpha,h}^{n+1}$, this step is completed. Within this update step, the vertical configuration is taken constant and equal to α_i^n, α_E^n . The whole step is shown in Figure 2, top right panel.

3.2 Removal/Insertion of top layers

Then we perform the insertion/removal of layers based on:

- 165 – An evaluation of the top layer indexes which become time-dependent. We call them the active ones $\alpha_{active} \subset \alpha$ and they have to be defined at nodes:

$$\alpha_{active,i}^{n+1} = \left\{ \alpha : z_{\alpha+1/2}^0 + \epsilon_{top} < \zeta_i^{n+1} \right\}, \quad \alpha_{top,i} = \min \alpha_{active,i} \quad (13)$$



and at elements:

$$\alpha_{active,E}^{n+1} = \left\{ \alpha : z_{\alpha+1/2}^0 + \epsilon_{top} < \min_{x \in E} \zeta_h^{n+1}(x) \right\}, \quad \alpha_{top,E} = \min \alpha_{active,E} \quad (14)$$

ϵ_{top} is a small and positive constant that fixes the minimum allowable depth for a top layer to exist. Below this threshold, the layer is too thin and it is removed. It turns out that this parameter is quite important since it avoids the presence of very thin layers, for which the vertical diffusion matrix becomes ill-conditioned. We have fixed it as $\epsilon_{top} = 0.2\Delta z_\alpha^0$.

170

- A conservative remap step is necessary to pass the solution obtained in the grid movement step on a grid with layers α_{active}^n to the new grid with layers α_{active}^{n+1} .

We use \tilde{u}_α^{n+1} to distinguish a generic layerwise variable remapped onto the new grid from the solution time stepped on the old grid u_α^{n+1} . This insertion/removal operation can be interpreted, at a continuous level, as an expansion/collapse of the

175 layer in a pseudo time (see the bottom-left panel in Figure 2). After the expansion/collapse, the interface location moves to

$z_{\alpha+1/2}^{n+1} \rightarrow \tilde{z}_{\alpha+1/2}^{n+1}$. Then, the remapped value is the solution of the following advection equation in a pseudo time:

$$\frac{\partial J \tilde{u}_\alpha}{\partial \tau} - J \frac{\partial \sigma \tilde{u}_\alpha}{\partial z} = 0$$

with J the Jacobian of the grid expansion/collapse and $\sigma = \frac{\partial z}{\partial \tau}$ the velocity of the grid. After integration over a layer:

$$\frac{\partial}{\partial \tau} \int_{\tilde{h}_\alpha(\tau)} \tilde{u}_\alpha dz = \left[\sigma \tilde{u}_\alpha \right]_{\alpha+1/2}^{\alpha-1/2}, \quad \sigma_{\alpha+1/2} = \frac{\partial z_{\alpha+1/2}}{\partial \tau}$$

In the discrete case, with a simple forward Euler (with initial condition $\tilde{u}_\alpha^n = u_\alpha^{n+1}$) and upwind flux, we get:

$$\tilde{h} u_\alpha^{n+1} = h u_\alpha^{n+1} + \Delta \tau \left[\sigma u_\alpha^{n+1} \right]_{\alpha+1/2}^{\alpha-1/2}, \quad \sigma_{\alpha+1/2} = \frac{\tilde{z}_{\alpha+1/2}^{n+1} - z_{\alpha+1/2}^{n+1}}{\Delta \tau} \quad (15)$$

We can apply such a remapping to the variables discretized on the horizontal grid u_h and for element removal/insertion operations. In the case of an element removal ($\alpha_{top,E}^{n+1} > \alpha_{top,E}^n$), we identify the layer that should disappear and we proceed with a collapse of the lower interface to the upper one. For the existing and removed layer, equation (15) reduces trivially to transfer the depth-integrated variable that belongs to the removed layers to the upper active layer. In the case of an element insertion ($\alpha_{top,E}^{n+1} < \alpha_{top,E}^n$), we identify the layer that should appear and we expand the interface. Then equation (15) reduces to distribute the depth-integrated variable across the existing and inserted layers. The same arguments can be applied to nodal variables, replacing $\alpha_{top,E}$ with $\alpha_{top,i}$.

185

3.3 Connection to z-surface-following coordinates

The vertical coordinate described so far is controlled by the parameter ϵ_{mov} that describes the number of moving surface layers. It is convenient to express this constant as a percentage of the z-layer depth at rest $\epsilon_{mov} = r_{mov} \Delta z_\alpha^0$. Due to the presence of the free surface (unknown at the beginning of the simulation) in (10), it is not easy, even for equispaced z-grid,

190

to find a simple formula that links r_{mov} to the number of moving layers N_{mov} . However, we can compute an estimate of the maximum free surface height during the simulation, $\max \zeta$, and use the relation (10) $r_\alpha = \frac{\max \zeta - z_{\alpha-1/2}^0}{\Delta z_\alpha^0}$ to state that:

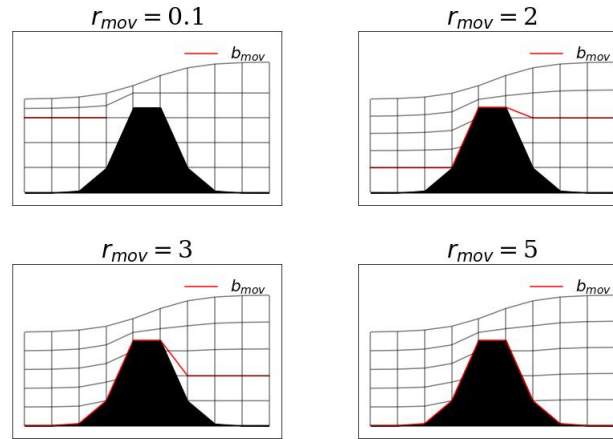


Figure 3. From top to bottom: different grids obtained in the vertical movement step with different r_{mov} . In red is the highlighted the depth of the moving layers b_{mov} .

- $0 < r_{mov} \ll 1$ means that only the layers spanned by the free surface movement will undergo deformation. As we increase r_{mov} , the deformation becomes less local and more layers are progressively deformed.
- if we set $r_{mov} = r_{N_{mov}}$, we will move, at minimum, N_{mov} layers.
- 195 – if we increase the parameter beyond $r_{mov} > r_N$, then all layers are moving.

In Figure 3 we have plotted different grids obtained in the vertical movement step with a varying grid parameter r_{mov} and different corresponding moving surface layers N_{mov} .

The z-surface-adaptive coordinate and the z-surface-following coordinate are then obtained with the following choices:

- 200 – z-surface-adaptive: $r_{mov} \leq r_{top}$. The grid deformation is localized to the free surface. As long as elements are deformed, they are too small and immediately removed in the grid topology step. This implies working, at the next time step, with a true z-grid. We stress the importance of the grid movement step. Without such a step, it would be impossible to timestep the variables on layers with positive depth, with all the related stability issues, included for the tracer equation where you need layer thickness at t^n and t^{n+1} . One may think to compute the tracer after the insertion/removal operations have been performed (thus having positive layer thickness both at t^n and t^{n+1}), but in this way the configuration on which the discrete tracer equation is solved is ambiguous (it is the old or the new one?) and it seems hard to verify tracer constancy property.
- 205 – z-star: $r_{mov} > r_N$ and no insertion/removal. The whole water column is subjected to the grid movement while the number of layers does not change. These are z-star coordinates, or any z-surface-following coordinates depending on which coefficients $l_{\alpha,i}$ are plugged in equation (12).

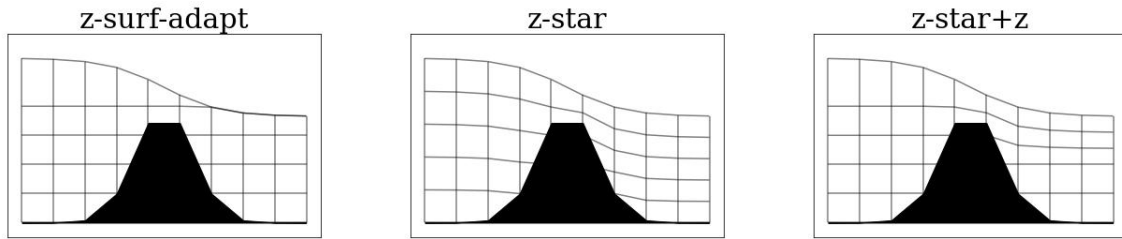


Figure 4. The different vertical z-grids outlined in Section 3.3.

210 – z-star+z: $r_\gamma = \frac{\max \zeta - z_\gamma^0}{\Delta z_\gamma^0} - 1/2$ and no insertion/removal. The upper part of the water column, at minimum γ layers, is subjected to the grid movement while the lower part is fixed. This corresponds to a partially z-star and partially z-system.

Figure 4 shows a sketch of the different possibilities.

4 Advection with spatially variable number of layers

We have used an approach where the grid topology does not change during the time step of the conserved variables, i.e. the scheme works on the deforming grid of Section 3.1, with a *temporally* constant number of layers between t^n and t^{n+1} . However, in the previous time step, a layer insertion/removal may occur (to remove very thin surface layers, or to split a thicker layer) on a certain element and not on its neighbors. This results in a grid with a *spatially* variable number of layers. Hanging interfaces appear for the top layers, see the top left panel of Figure (5). Some modifications have to be implemented to deal properly with such hanging interfaces, see on this topic Bonaventura et al. (2018).

220 Consider the example in Figure (5) where two contiguous elements with different top-layer index $\alpha_{top,i+1/2} > \alpha_{top,i-1/2}$ exist. In correspondence with node i we have a non-conformal vertical edge with two hanging layers which slightly sophisticate the treatment of advection terms. In our case, with only insertion/removal of surface layers, we can easily flag boxes that deserve a special treatment by checking, for each element, that the nodal top layer index is different from the elemental one:

$$\text{if } \alpha_{min,E} < \alpha_{top,E} \quad \text{then} \quad E = E^*$$

with $\alpha_{min,E} = \min_{j \in E} \alpha_{top,j}$. Then the boxes called hereinafter for simplicity "non-conformal" can be identified by the pair of index $(\alpha_{top,E}, E^*)$. Since horizontal and vertical advection terms/fluxes need communication with the neighbors' boxes, they have to be treated differently.

Moreover, for the tracer discrete update, we have to take care of preserving the **constancy** property. The key ingredient to verify tracer constancy for a hydrostatic numerical model is that the tracer discrete update, in case of a constant solution, collapses to the discrete layerwise mass conservation. The last is always verified because it is used to compute the mass-transfer function. Assuming that the time derivative and the vertical advection terms in (6) and (7) are treated equally, it is enough to verify that the horizontal advection term reduces to the mass-flux term, also for non-conformal boxes. However, the practical

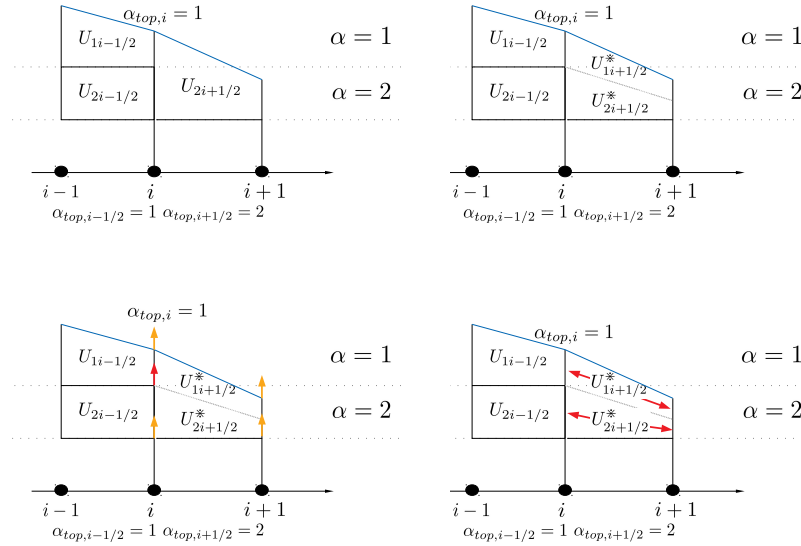


Figure 5. Treatment of non-conformal box. Top left: non-conformal box. Top right: splitting with fictitious layers. Bottom left: mass-transfer function $G_{1+1/2,i}$ at hanging node is represented by a red arrow. Bottom right: horizontal advection terms $f_{2,i}, f_{2,i+1}$ and $f_{1,i}, f_{1,i+1}$ computed for each fictitious layer are represented by red arrows.

implementation depends on the specific numerical scheme. In the next paragraph, we show the case of a B-type staggered finite element discretization as the one used in the SHYFEM model.

4.1 Case of staggered Finite-Element on a B-grid

235 We consider a discretization where the water levels and the momentum (transports) are described using functions of different order and support. Momentum is approximated through:

$$hu_{\alpha,h}(x,t) = \sum_{E=1,M} \psi_E(x) hu_{\alpha,E}(t) \quad (16)$$

with $\psi_E(x) \in E$ the constant piecewise functions and $hu_{\alpha,E}(t)$ the elemental momentum. The elemental cur are obtained from $u_{\alpha,E} = \frac{hu_{\alpha,E}}{h_{\alpha,E}}$. For the free surface, given an approximation of nodal values $\zeta_i(t) = \zeta(x_i,t)$, we introduce a continuous numerical approximation:

$$\zeta_h(x,t) = \sum_{i=1,M+1} \varphi_i(x) \zeta_i(t) \quad (17)$$

240 $\{\varphi_i\}_{i=1,M+1}$ is the standard P^1 continuous piecewise linear Lagrange kernel. Tracers are approximated with the same formula (17), $t_{\alpha,h}(x,t) = \sum_{i=1,M+1} \varphi_i(x) t_{\alpha,i}(t)$. A sketch of the vertical grid is reported in Figure (6).

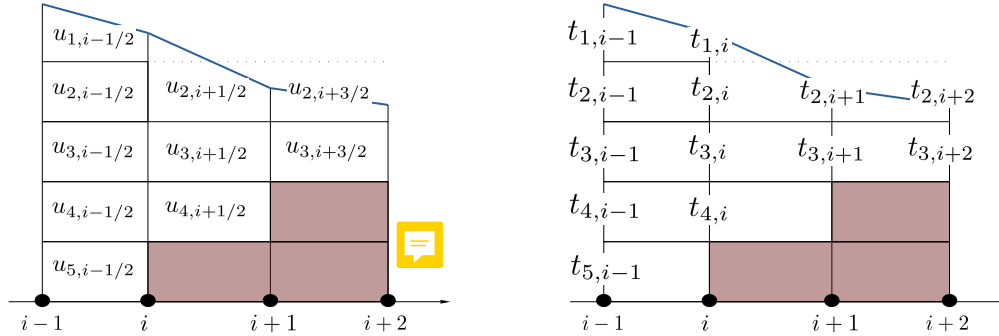


Figure 6. Sketch of the staggered grid with elemental velocities and nodal tracers values.

We obtain the weak formulation multiplying the governing equation by a test function that belongs to the same space of the solution and integrating it in the computational domain. Then, the finite element discretization of the mass-flux term in the layerwise mass equation (6) is computed, for each element, after integration by part:

$$\int_{\Delta x_{i+1/2}} \frac{\partial \varphi_i}{\partial x} h u_{\alpha,h} dx = a_{i,i+1/2} h u_{\alpha,i+1/2}$$

245 with the coefficient:

$$a_{i,i+1/2} = \int_{\Delta x_{i+1/2}} \frac{\partial \varphi_i}{\partial x} dx$$

For the computation of horizontal advection we consider the tracer equation. The elemental contribution to the advection term reads, after integration by parts:

$$\int_{\Delta x_{i+1/2}} \frac{\partial \varphi_i}{\partial x} h u_{\alpha,h} t_{\alpha,h} dx = \sum_{j=i,i+1} k_{\alpha,ij} t_{\alpha j} = f_{\alpha i}^{i+1/2}$$

with the coefficient:


$$k_{\alpha,ij} = \int_{\Delta x_{i+1/2}} \frac{\partial \varphi_i}{\partial x} \varphi_j dx h u_{\alpha,i+1/2} \quad (18)$$

We consider any P^1 stabilized method written in the form (neglecting the subscript α in the matrix entries):

$$f_{\alpha i}^{i+1/2} = \sum_{j=i,i+1} (k_{ij} + d_{ij}) t_{\alpha j} \quad (19)$$

250 with d_{ij} a consistent discrete stabilization operator which has to be symmetric with zero row sum $\sum_{j=i,i+1} d_{ij} = -d_{ii}$ (Kuzmin and Turek, 2002). For instance, d_{ij} can be the discrete Laplacian, the streamline-diffusion operator or, as in SHYFEM model,



a first-order upwind dissipation plus a second-order TVD correction tuned by a flux limiter, see  Kuzmin and Turek (2002).

In case of a non-conformal box we proceed as follows. First, we split the box vertically in $\alpha_{top,E} - \alpha_{min,E} + 1$ fictitious layers through planar interfaces passing through the hanging points of non-conformal edges and some fraction of the conformal edge length, see Figure (5), top right panel. Then we distribute the momentum of the top layer among the fictitious layers:

$$hu_{\alpha,E}^* = hu_{\alpha_{top,E},E} l_{\alpha,E}^* \quad \alpha = \alpha_{top,E}, \dots, \alpha_{min,E} \quad (20)$$

with $l_{\alpha,E}^* = \frac{h_{\alpha,E}^*}{h_{\alpha_{top,E},E}}$ and $h_{\alpha,E}^*$ the fictitious layer thickness. Finally, these values are used to complete both vertical and horizontal advection for the missing layers of non-conformal boxes (see Figure 5, bottom panels). Without loss of generality, we consider the case of node i sharing a non conformal right box $(i + 1/2, \alpha_{top,i+1/2})$, as in Figure (5). After the splitting (20), the mass-flux term reads:

$$\int_{\Delta x_{i+1/2}} \frac{\partial \varphi_i}{\partial x} hu_{\alpha,h}^* dx = c_{\alpha,i}^* a_{i,i+1/2} hu_{\alpha_{top,i+1/2},i+1/2} \quad \alpha \leq \alpha_{top,i+1/2} \quad (21)$$

with

$$c_{\alpha,i}^* = \begin{cases} \sum_{\beta=\alpha_{top,i}}^{\alpha_{min,i+1/2}} l_{\beta,i+1/2}^* & \text{if } \alpha = \alpha_{top,i} \text{ and } \alpha_{min,i+1/2} < \alpha_{top,i} \\ l_{\alpha,i+1/2}^* & \text{otherwise (hanging layer)} \end{cases} \quad (22)$$

where the two cases account for the contribution of element $i + 1/2$ to both nodes with and without hanging layers, respectively node i and $i + 1$ in Figure (5). The horizontal advection scheme (19) on the non-conformal box can be applied straightforwardly to the fictitious layers with modified coefficients $k_{\alpha,i,j} = l_{\alpha,i+1/2}^* k_{\alpha_{top,i+1/2},ij}$. Then, the advection term in non-conformal boxes reads (neglecting for simplicity the stabilization operator):

$$f_{\alpha,i}^{*i+1/2} = \begin{cases} \sum_{\beta=\alpha_{top,i}}^{\alpha_{min,i+1/2}} \sum_{j=i,i+1} l_{\beta,i+1/2}^* k_{\alpha_{top,i+1/2},ij} t_{\beta^*,j} & \text{if } \alpha = \alpha_{top,i} \text{ and } \alpha_{min,i+1/2} < \alpha_{top,i} \\ \sum_{j=i,i+1} l_{\alpha,i+1/2}^* k_{\alpha_{top,i+1/2},ij} t_{\alpha^*,j} & \text{otherwise (hanging layer)} \end{cases} \quad (23)$$

Again we have separated the cases of a node with/without hanging layers. Note that the subscript $(\alpha^*, j) = (\max(\alpha, \alpha_{top,j}), j)$ avoids selecting tracer values in removed layers.

The splitting of non-conformal boxes and the consequent treatment of advection terms for such boxes allows simple verification of the tracer constancy also in presence of a spatially variable number of layers. We have already mentioned that it is enough to verify that the horizontal advection term reduces to the mass-flux term, also for non-conformal boxes. We can verify this property by element. For a constant tracer ($t_{\alpha} = 1$), we write the advection term for a non-conformal box (23) as:

$$f_{\alpha,i}^{*i+1/2} = \begin{cases} \sum_{\beta=\alpha_{top,i}}^{\alpha_{min,i+1/2}} l_{\beta,i+1/2}^* \sum_{j=i,i+1} k_{\alpha_{top,i+1/2},ij} & \text{if } \alpha = \alpha_{top,i} \text{ and } \alpha_{min,i+1/2} < \alpha_{top,i} \\ l_{\alpha,i+1/2}^* \sum_{j=i,i+1} k_{\alpha_{top,i+1/2},ij} & \text{otherwise} \end{cases}$$



Through the definitions (22) and (18), it can be simplified to:

$$f_{\alpha,i}^{*i+1/2} = c_{\alpha,i}^* \sum_{j=i,i+1} k_{\alpha_{top,i+1/2},ij} = c_{\alpha,i}^* a_{i,i+1/2} h u_{\alpha_{top,i+1/2},i+1/2}$$

which is the discrete mass-flux for non-conformal box (21). This completes the tracer constancy verification.

275 5 Numerical tests

All the tests have been run with the ocean model SHYFEM which is based on the Finite Element procedure of Section 4.1 applied to unstructured triangular grids. The extension of the z-surface-adaptive algorithm to unstructured grids is straightforward. In particular, nodal definitions apply identically and elemental definitions apply to triangular elements K . SHYFEM uses a semi-implicit method to march variables in time.

280 5.1 Impulsive Wave

As the first test, we check the accuracy of the z-surface-adaptive coordinate with an increasing vertical resolution. We use a closed basin $[-5, 5] \times [-5, 5]$ with constant depth $b = 1$. The basin is initially at rest and the free surface is perturbed by the following Gaussian hump:

$$\zeta(x, y, t = 0) = A \exp(-r^2/\tau)$$

285 with $A = 1/2$, $\tau = 1/2$ and $r = \sqrt{x^2 + y^2}$. A constant passive tracer is prescribed on the background and such a constant state should be preserved along the simulation. The mesh has a horizontal element size of $h_K = 0.25$. We compare different vertical resolutions with variable layer thicknesses. The coarsest grid has three layers: a first top layer with thickness of $\Delta z_1 = 0.2$, the second and the third layers have thicknesses of $\Delta z_{2,3} = 0.4$. The other vertical grids are obtained by halving each of these layers. The finest grid has 24 layers with minimum layer thickness at the surface of $\Delta z = 0.025$.

290 Without bottom/surface forcing, if the initial currents are constant along z, they must remain barotropic and equal to the depth-integrated currents of the Shallow Water equations (1-layer case). Of course, this is not a property of the discrete z-coordinate scheme (but the scheme should converge to a barotropic solution refining the resolution). It is however desirable that the results of 2d and 3d models are similar for the typical resolution of an ocean simulation (Kleptsova et al., 2010). The 1-layer discrete solution is considered here as a reference solution against which we compare our implementation of the z-layers. The coarse grid with 3-layer is also used for comparison since the free surface is always contained in the first layer and no insertion/removal is necessary. For the 24-layer grid, up to six layers are progressively removed (and then re-inserted). In Figure (7), all resolutions show a good agreement for both the water level and the barotropic current. We can check some conservation properties of the scheme. As usual for such an adaptation strategy, mass is conserved up to machine precision (SHYFEM is coded in single-precision). This is what we check in Figure (8), left panel, where no source of mass error is present with respect to the 3-layer case. A direct consequence of mass conservation is tracer constancy preservation, up to
300 machine precision, Figure (8), right panel.

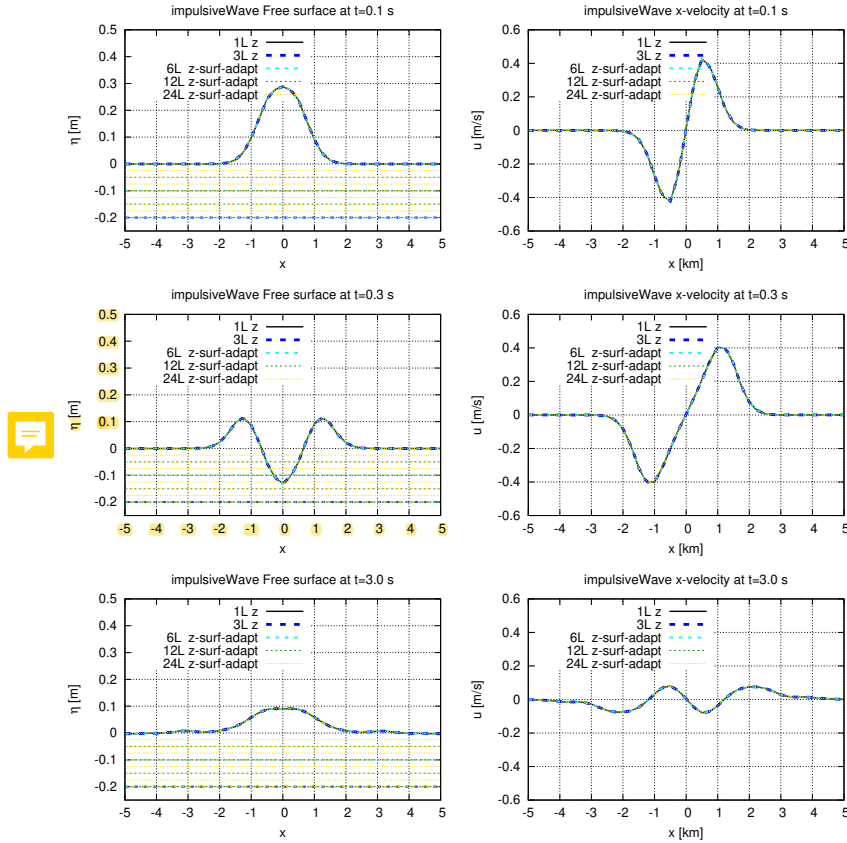


Figure 7. Impulsive Wave. Comparison of free surface and barotropic currents for different vertical grids. For each grid the z-interfaces are traced with dashed lines.

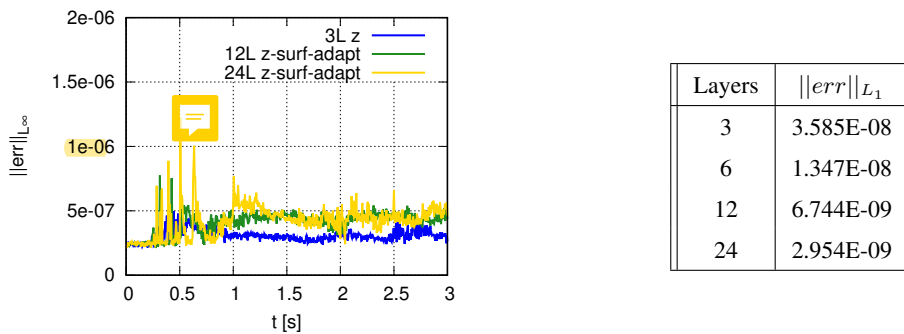


Figure 8. Impulsive Wave. Left: relative mass conservation error for a fluid box $err = \int_{\Delta x} \Delta h_{\alpha,h} dx - \Delta t \left([hu_h]_i^{i+1} - \int_{\Delta x} [G_h]_{\alpha+1/2}^{\alpha-1/2} dx \right)$. Right: relative tracer conservation error $err = T - T_0$ at final time $t = 3$.



5.2 1-d tidal flow in a sloping channel

Coastal applications include extensive intertidal flats. As with many ocean models, SHYFEM handles wetting and drying processes in a simplified manner, applying ad-hoc treatments in dry cells. An extrapolation algorithm for the free surface is used to track the shoreline and identify dry and wet regions. Then, the two regions are treated separately, see Umgiesser (2022) for the details. The test that we propose, presented in Oey (2005), is a benchmark for wetting/drying algorithms used in ocean models. The domain consists of a 1d sloping channel that ranges from $x = 0\text{km}$ at the landward end to $x = 25\text{km}$ at the seaward boundary. The slope of the bathymetry is $b(x) = 10x/(25\text{km})$. The horizontal mesh size is equal to $h_K = 250\text{m}$. A periodic water level is imposed at the seaward boundary $\zeta = 10(1 - \sin(10\pi t))$. At the beginning of the simulation, the channel is dry. Typically this test is run with 1-layer models (Warner et al., 2013). Here we use the 1-layer solution (1L) as a reference and we test the 5-layer with surface-adaptation and the 5-layer with z-star. In the 5L z-surface-adaptive simulation, only one layer is present at the beginning of the simulation and then, as long as the free surface is tilted by the boundary signal, more levels are inserted and then removed during the drying phase. Flooding is thus performed with a 1-layer Shallow Water model with the classical wetting/drying algorithms that may be deployed in dry or nearly dry areas (e.g. positivity limitation, momentum regularization, etc...). With z-star instead, such wetting and drying algorithms are applied to all layers.

In Figure (9) we check the along-channel solution profiles. Despite the different manner of handling wetting/drying for the 5L z-surface-adaptive and 5L z-star simulations, a quite good agreement is observed for the free surface, while larger differences are found for the barotropic current where both the 5-layers simulations appear noisier at the wet/dry interface.

5.3 Venice Lagoon idealized test

Here we test the different z-coordinates in a realistic lagoon environment forced by the tidal oscillation. The Venice Lagoon is characterized by a complex system of shallow areas subjected to wet-dry processes (the average basin depth is of the order of 1m) and deeper channels (maximum depth around 15m). We simulate a summer period when the strong diurnal heating sums up river runoff and make the lagoon less dense than the sea-water entering from the inlets. The flow is mainly driven by the tidal currents that transport water masses with different densities along the lagoon channels. The deeper channels can experience surface stratification during summer.

In this test, the lagoon is forced with analytical functions representative of a calm summer period characterized by strong solar radiation. The vertical eddy viscosity μ_v and the vertical tracer eddy diffusivity μ_{tv} are computed with the turbulence module GOTM (Buchard et al.). At the inlets, the lagoon is forced with a semi-diurnal tidal signal with amplitude 0.4m and period 12 hours, sea-water at $T = 25^\circ\text{C}$ and $S = 35\text{PSU}$. The lagoon is initialized with constant temperature $T = 25^\circ\text{C}$ and salinity $S = 30\text{PSU}$. The simulation lasts ten days.

A coarse horizontal grid made out of 7842 triangular elements and 4359 nodes is used. This grid however is capable of representing the main channels and islands where smaller elements are placed (Figure 10). We consider two vertical resolutions summarized in Table 11. The deeper part (from the bottom to -2m from the reference level) is equal for the two z-grids and it is composed of 16 levels with variable thicknesses, going from $\Delta z = 0.5$ near the surface up to $\Delta z = 4\text{m}$ at 40m. The

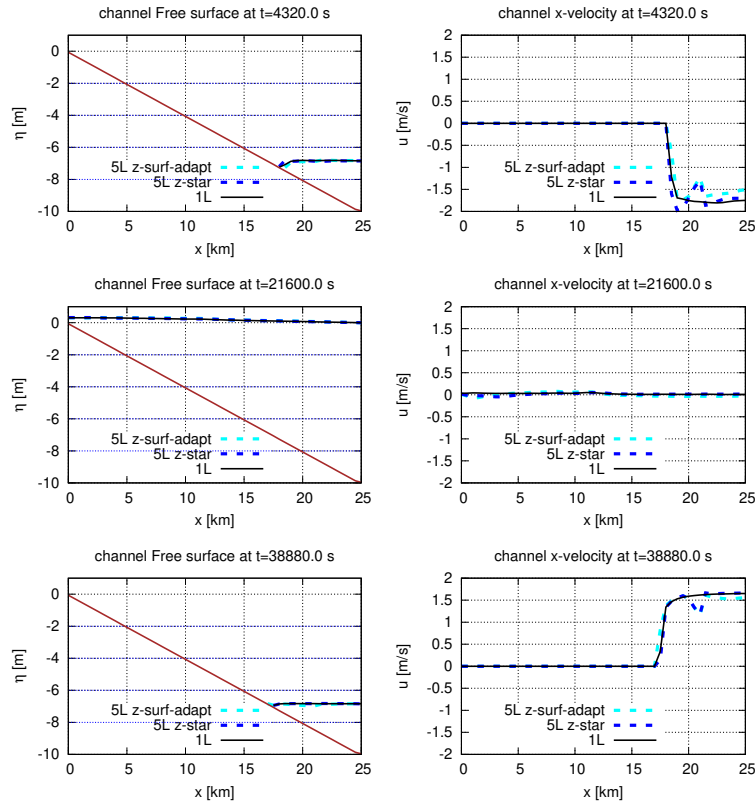


Figure 9. 1d tidal channel flow. Comparison between the 1-layer and 5-layers z-grids. Left: of free surface. Right: barotropic currents. Dashed blue lines represent the interfaces of the 5 layer z-grid.

335 resolution of the upper part of the water column differs: the coarse grid has the first layer of $\Delta z_1 = 1$ m followed by two layers
 with a thickness of $\Delta z = 0.5$ m. This choice avoids the drying of the first layer. In the upper part, the fine grid has 8 layers
 with a constant thickness of $\Delta z = 0.25$ m. Three simulations have been performed: a coarse one with standard z-coordinate
 (19L z), a fine one with z-surface-adaptive coordinate (24L z-surf-adapt) and a fine one with z-star (24L z-star). Given the
 fine vertical resolution and the tidal amplitude of 0.4 m, the 24L z-surf-adapt simulation should undergo extensive element
 340 insertion/removal. In the right picture of Figure 11 we have reported the time evolution of the number of elements inserted and
 removed during two tidal periods. More than 150 surface elements happened to be inserted or removed in a single time step.

In Figure 12, we show the free surface and the barotropic velocity recorded at two stations, at "Punta della Salute" in Venice,
 quite close to the northern inlet and at "Canale dei Petroli" placed in the deep tanker ship channel, (named respectively G2 and
 G8 in Figure 10). The signals of the three simulations are almost overlapping with small differences in the velocities.

345 **Always** the stations G2 and G8 we show the velocity and tracer profiles. At the station G2, in Figure 13, the tracer profile
 is mostly well-mixed. At station G8, in Figure 14, we observe that the ebb phase is followed by a stratification of the water
 column which is then erased after the flood phase. First, we note that the vertical resolution seems to strongly affect the tracer

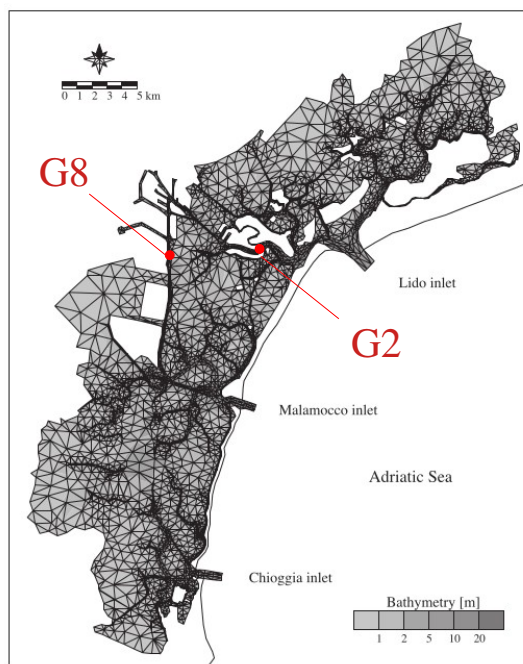


Figure 10. Venice lagoon. Horizontal grid and tidal stations.

COARSE (19L)	FINE (24L)
	0.25
1	0.25
	0.25
	0.25
0.5	0.25
	0.25
0.5	0.25
	0.25
0.5	0.5
...	...
Deeper water with variable	$0.5 < \Delta z < 4$

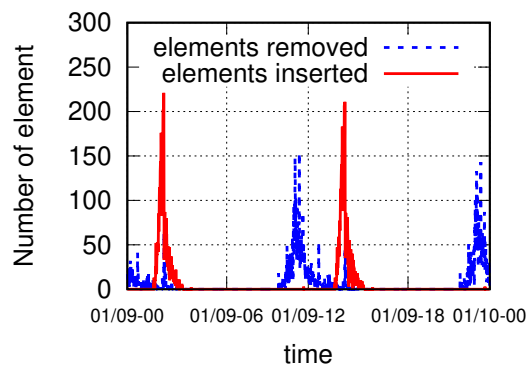


Figure 11. Venice lagoon. Left: coarse (19 layers) and fine (24 layers) vertical z-grids. Right: time evolution of total number of layer inserted and removed per time step for the 24L-z simulation.

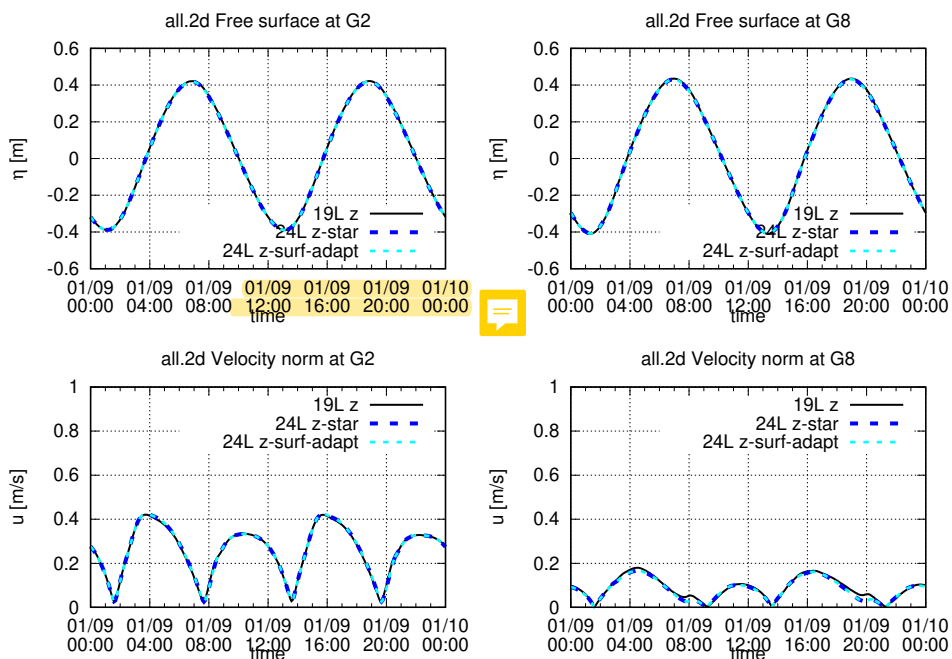


Figure 12. Venice lagoon. Free surface and barotropic velocity norm at stations G2 and G8

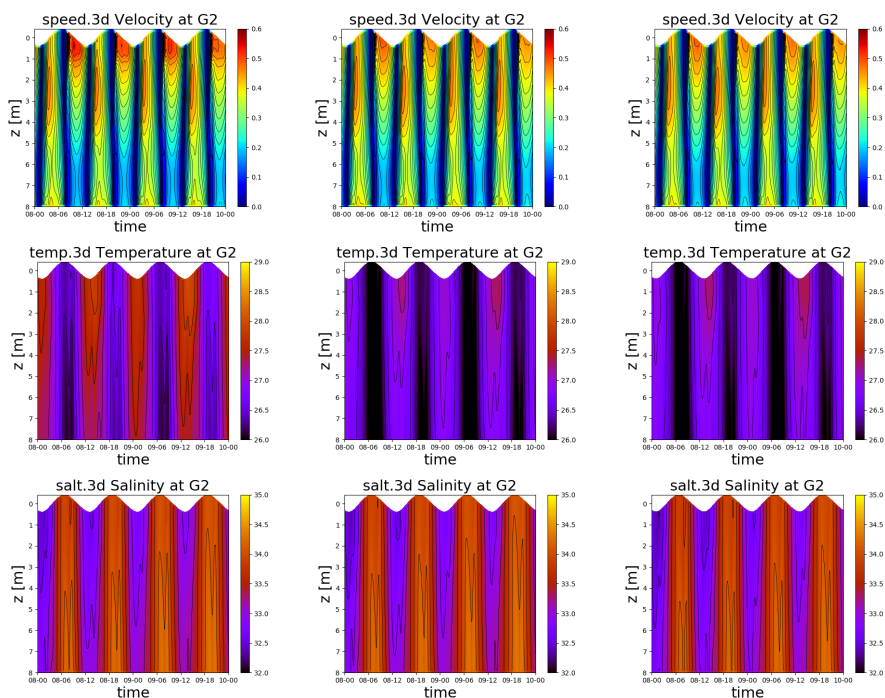


Figure 13. Venice lagoon. Current, temperature and salinity profiles at station G2. Left: 19L z. Middle: 24L z-surf-adapt. Right: 24L z-star.

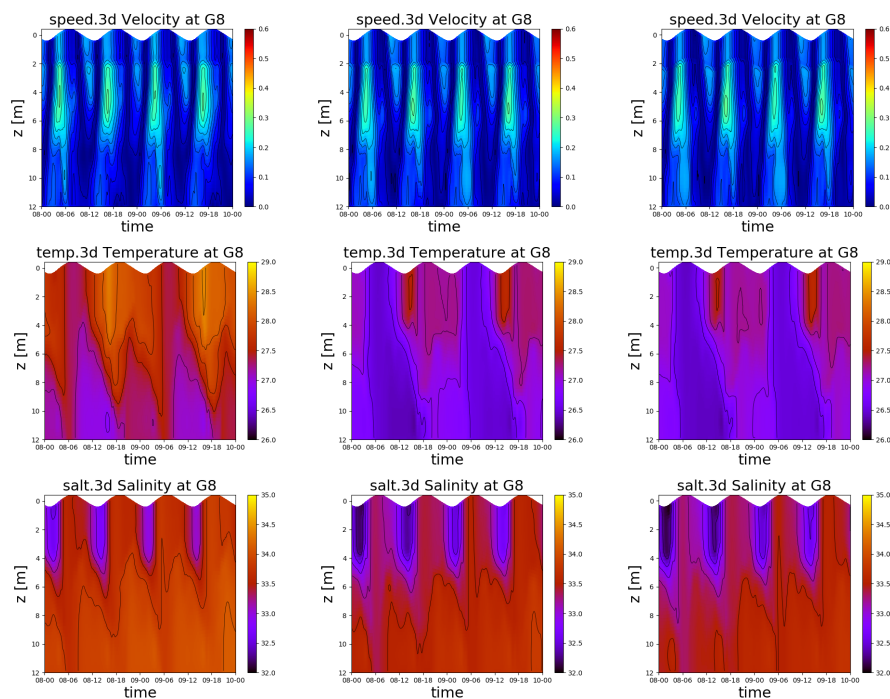


Figure 14. Venice lagoon. Current, temperature and salinity profiles at station G8. Left: 19L z. Middle: 24L z-surf-adapt. Right: 24L z-star.

evolution. Although the coarse and fine simulations show similar periodic profiles, the 19L z simulation shows significantly lower temperatures. For the temperature, we believe this is due to the different mechanisms of heating and cooling. Heating is mainly associated with the incoming short-wave solar radiation which acts as a body force for the upper water column. On the contrary heat loss through latent and sensitive heat flux occurs via a boundary condition (in a layerwise model, a source term for the first layer only). Thus the first layer thickness strongly impacts the temperature evolution, in particular in our case a thinner layer causes a more rapid cooling during the night, which leads the lagoon to a colder state. Second, comparing the two fine simulations (24L z-surf-adapt and 24L z-star), we found that they are in close agreement which seems to confirm the analysis of Section 2 (see also the Appendix): for micro-tidal applications and fine vertical resolutions, the mixing related to the free surface oscillation is small.

We report the CPU time of the three serial simulations which have been run on a modern workstation with a AMD EPYC 7643 Processor : 7099 s (19L z), 12227 s (24L z-star), 13261 s (24L z-surf-adapt) showing an overhead of around 8% for the insertion/removal operations.

360 6 Conclusions

In this work, we have reviewed the performances of geo-potential coordinates for the simulation of free surface coastal flows. We have investigated a well-known issue of geo-potential coordinates when incorporating the free surface: the limitation on



the resolution of the surface layer thickness. We have proposed a flexible algorithm based on a vertical adaptation to the tidal oscillation called *z-surface-adaptive*. With a dynamic insertion and removal of surface layers, the grid (at least the internal
365 interfaces) is always aligned to geo-potential, canceling the pressure gradient error. Thanks to a two-step procedure (vertical grid movement of surface layers followed by the insertion/removal operations), this algorithm preserves the stability and conservation property of the numerical scheme. As a particular case, the algorithm can be reverted to *z-surface-following* coordinates, such as the popular *z-star*.

Without the limitation on the surface resolution, we have been able to compare the *z*-coordinate with insertion/removal
370 (surface-adaptive) against *z-star* for typical coastal applications of semi-enclosed shallow seas with a tidal signal imposed at the openings and wetting/drying at intertidal flats. The comparison has been carried out with numerical experiments and simple analysis. In particular, using a local truncation error analysis we have investigated the additional numerical mixing associated with *z*-coordinates with the free surface. The analysis shows that, for high tidal ranges, the *z*-coordinate may suffer from spurious mixing or even from over-compressive effects, depending on the resolution and the flux limiter. However, as to be
375 expected intuitively, we have found that, for micro-tidal ranges and typical vertical resolutions of coastal models, these errors are small. In such conditions, with a simulation of the Venice Lagoon circulation, we shows that surface-adaptive-*z* coordinates can be used without a significant loss of accuracy.

Code and data availability. The SHYFEM hydrodynamic model is open source (GNU General Public License as published by the Free Software Foundation) and freely available through GitHub at <https://github.com/SHYFEM-model>. The current developments have been
380 implemented in a branch of SHYFEM v. 7_5_71 that can be accessed from Zenodo (Arpaia, 2023, <https://doi.org/10.5281/zenodo.7528681>). Configuration files and data used to run each test case are also available at the same Zenodo repository.

Appendix A: Numerical mixing induced by a tidal flow

We derive a closed-form expression for the numerical mixing of *z*-coordinate layerwise models when large vertical velocities associated with tidal flows are present (Klingbeil et al., 2018). To simplify the analysis we assume the case of a passive tracer
385 advected by a barotropic linearized flow with water depth $H(x, t)$ and barotropic velocity $u(x, t)$. We note that, for surface-following coordinates, the mass-transfer function (6) is zero (because of $h_\alpha = l_\alpha H$). The layers are thus aligned along the materials and the tracer is just advected along a layer without any discretization error arising from the vertical approximation. For this reason, hereinafter in the section, we take the *z-star* coordinate as the reference solution. On the contrary for *z*-coordinate models, the mass-transfer is the vertical velocity, a linear function of depth:

$$G_{\alpha-1/2} = -w_{\alpha-1/2} = \frac{\partial u}{\partial x} \sum_{\beta=N}^{\alpha} h_\beta \quad (\text{A1})$$



390 Then, the vertical advection fluxes will trigger some numerical noise (diffusion or dispersion). For a linearized barotropic flow, we can use the mass equation $\partial_t \zeta + H_0 \partial_x u = 0$ to replace:

$$\left| \frac{\partial u}{\partial x} \right| = \frac{1}{H_0} \left| \frac{\partial \zeta}{\partial t} \right| \leq \frac{A\Omega}{H_0} \quad (\text{A2})$$

with A the tidal amplitude, $\Omega = 2\pi/T$, T the tidal period and H_0 the bottom depth.

The exact solution satisfies the layer-averaged continuous conservation law:

$$\frac{\partial t_\alpha^{ex}}{\partial t} \Big|_s + \frac{\partial ut_\alpha^{ex}}{\partial x} + \frac{\overline{\partial wt^{ex}}}{\partial z} = 0$$

where $t_\alpha^{ex} = \overline{t^{ex}}$ and the average operator is $\overline{(\cdot)} = h_\alpha^{-1} \int_{z_{\alpha+1/2}}^{z_{\alpha-1/2}} (\cdot) dz$. The local truncation error (LTE) measures the error introduced by the numerical method, in our case the vertical discretization only. We define it after applying the true solution to the layerwise conservation for the tracer (7) restricted to the grid points z_α (the diffusion term is not considered):

$$\frac{\partial t_\alpha^{ex}}{\partial t} \Big|_s + \frac{\partial ut_\alpha^{ex}}{\partial x} + \frac{1}{h_\alpha} [wt^{ex}]_{\alpha+1/2}^{\alpha-1/2} + LTE_\alpha = 0 \quad (\text{A3})$$

Since we have used the layer-integrated form of the conservation law, we have divided it by the layer depth, which is constant for internal z-layers. After canceling common terms:

$$LTE_\alpha = \frac{\overline{\partial wt^{ex}}}{\partial z} - \frac{1}{h_\alpha} [wt^{ex}]_{\alpha+1/2}^{\alpha-1/2} \quad (\text{A4})$$

where the numerical fluxes at the interfaces are computed with the TVD scheme (8). In our time-continuous analysis $\Delta t \rightarrow 0$, (8) corresponds to combine an upwind flux formula with a second-order centered flux:

$$w_{\alpha-1/2} t_{\alpha-1/2} = w_{\alpha-1/2}^+ t_\alpha + w_{\alpha-1/2}^- t_{\alpha-1} + \frac{|w_{\alpha-1/2}|}{2} (t_\alpha - t_{\alpha-1}) \phi_{\alpha-1/2}$$

We recall that $\phi_{\alpha-1/2} = \phi(r_{\alpha-1/2})$ is the Superbee limiter and r is a measure of the smoothness of the tracer profile. Typically the solution is expanded in a Taylor series about z_α :

$$t^{ex}(z) = t_\alpha + \frac{\partial t}{\partial z} \Big|_\alpha (z - z_\alpha) + \frac{1}{2} \frac{\partial^2 t}{\partial z^2} \Big|_\alpha (z - z_\alpha)^2 + \frac{1}{6} \frac{\partial^3 t}{\partial z^3} \Big|_\alpha (z - z_\alpha)^3 + O((z - z_\alpha)^4)$$

We consider a z-grid with uniform vertical grid spacing h . Note that, for a z-grid, the first layer cannot have the same thickness as other layers but this makes the analysis more complex, so we restrict to equispaced internal layers. We replace the expanded expression of the true solution into the definition (A4), see e.g. Nishikawa (2020). After some algebra, we get (only leading order diffusive terms shown):

$$LTE_\alpha = \frac{1}{2} ((|w_\alpha| - (|w|\phi)_\alpha) \frac{\partial^2 t}{\partial z^2} \Big|_\alpha h + \frac{1}{6} |[w]| \frac{\partial^2 t}{\partial z^2} \Big|_\alpha h + O(h^3))$$

where w_α is the vertical velocity at the layer mid-point and $[w]_{\alpha+1/2}^{\alpha-1/2}$ is the difference over the layer. We collect the diffusive terms and replace the expression for the vertical velocity (A1):

$$D_\alpha^{num} = \frac{1}{2} \left(\left| \frac{\partial u}{\partial x} \right| \left((b + z_\alpha) - ((b + z)\phi)_\alpha \right) \frac{\partial^2 t}{\partial z^2} \Big|_\alpha h + \frac{1}{6} \left| \frac{\partial u}{\partial x} \right| \frac{\partial^2 t}{\partial z^2} \Big|_\alpha h^2 + O(h^3) \right)$$



Finally using the upper bound (A2) and $(b + \zeta)/H_0 \approx 1$ we get:

$$D_{\alpha}^{num} \leq \frac{1 - \phi_{\alpha}}{2} A \Omega \frac{\partial^2 t}{\partial z^2} \Big|_{\alpha} h + \frac{1}{6} \frac{A \Omega}{H_0} \frac{\partial^2 t}{\partial z^2} \Big|_{\alpha} h^2 + O(h^3) \quad \square$$

410 We perform here a simple experiment in a coastal environment (depth $H_0 = 50$ m and $\Omega = \frac{2\pi}{12.41 \text{ hours}}$) with two smooth tracer profiles, an exponential one $t(z) = t_0 \exp\{-z/\Lambda\}$ with small vertical derivatives ($\Lambda = 100$) and a hyperbolic tangent $t(z) = t_0 + \alpha \tanh\{(z + z_0)/\Lambda\}$ which exhibits larger vertical derivatives at the surface ($\Lambda = 2$). We consider a constant tracer diffusivity $\nu_{tv} = 5e - 5$. In Figure A1 we compare the L2-norm of the two contributions, $\|D_{\alpha}^{phy}\|$ and $\|D_{\alpha}^{num}\|$, the latter divided in a diffusive and anti-diffusive contribution. Different tidal amplitudes and vertical resolutions are investigated. To
415 confirm the theoretical results we compute also the solution numerically with SHYFEM using the same vertical data and numerics of the analytical case. The numerical experiment has been carried out in a one-dimensional basin 21 km long with a mesh size of 50 m and a time step of 120 s. The numerical tracer profile is evaluated after 5 tidal periods. In Figure A1 the z-coordinate numerical profiles are compared against the reference z-star numerical profiles.

For the exponential profile, in the top panel of Figure A1, both the theoretical and the experimental numerical mixing are
420 very small compared to the physical mixing. Only at large resolution and for large tidal amplitude does the numerical diffusion reaches the same order as the physical one and the profile starts to be slightly smeared out at the surface. Since the limiter is, at all depths, close to one such a diffusive effect could be attributed, from our analysis, to the second-order term. The situation changes for the hyperbolic tangent profile in the bottom panel of Figure A1. The limiter is active at the surface and introduces first-order diffusion which, at low resolution, overtakes the physical diffusion making the profile very smeared out. At finer
425 resolutions the numerical mixing reduces and it becomes negligible for all tidal amplitude with $h \leq 2.5$ m. At such resolutions the profile follows well the reference solution, although, for large tidal amplitudes, the anti-diffusive term is large and a small overcompression of the profile can be observed at the surface.

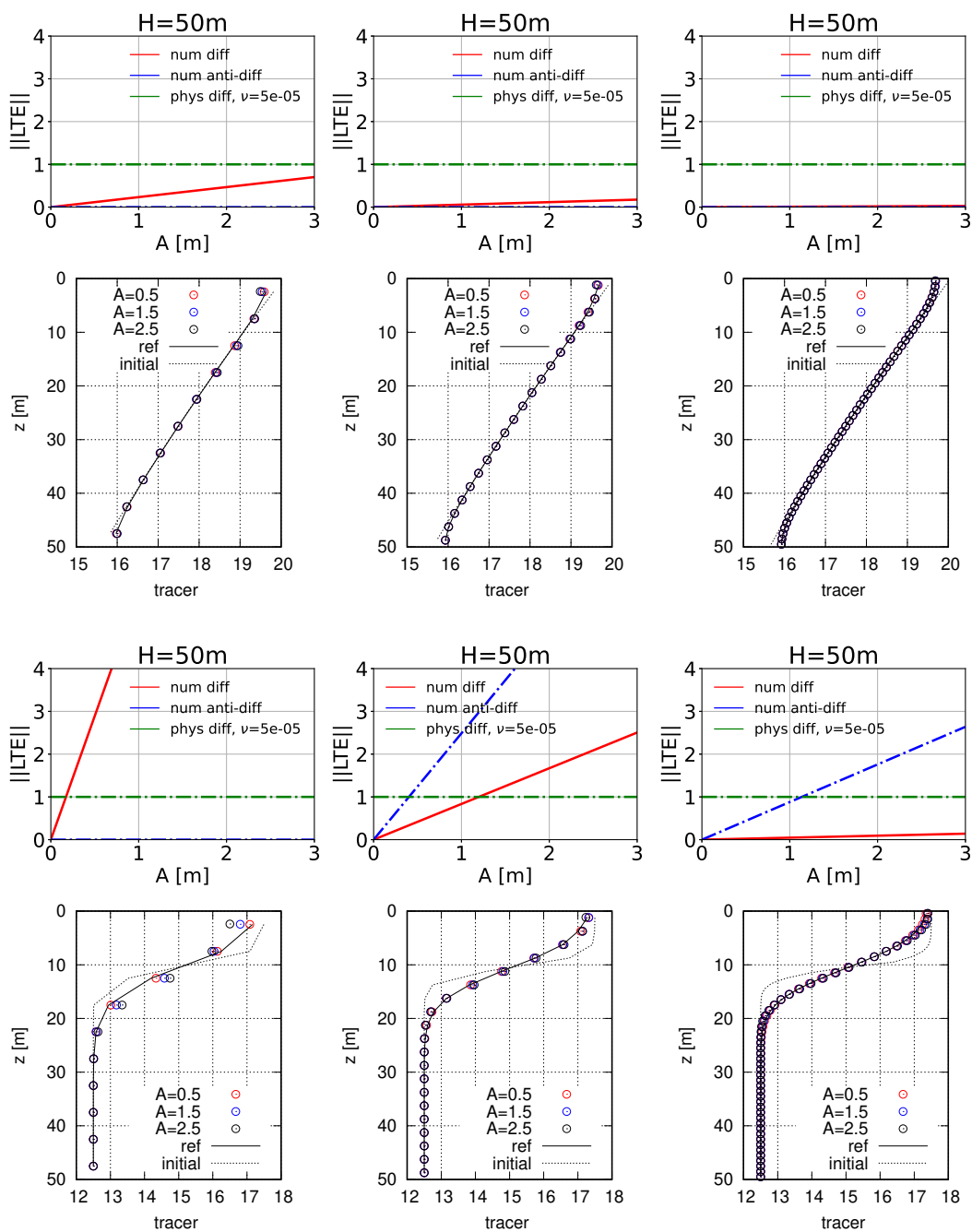


Figure A1. Smooth stratification experiment. Top: numerical mixing (normalized by physical mixing) for different tidal amplitudes. Bottom: Numerical tracer profiles computed with SHYFEM for different tidal amplitude. From left to right: increasing vertical resolution, $h = 5m$, $h = 2.5m$, $h = 1m$



Author contributions. L. Arpaia: Conceptualization, Methodology, Software, Validation, Writing, Formal analysis. C. Ferrarin: Conceptualization, Methodology, Funding acquisition, Writing, Resources, Validation. M. Bajo: Methodology, Writing. G. Umgiesser: Conceptualization, Methodology, Writing, Software.

430

Competing interests. The authors declare that they have no known competing financial interests or personal relationships that could have appeared to influence the work reported in this paper.

Acknowledgements. This work was partially supported by the project AdriaClim (Climate change information, monitoring and management tools for adaptation strategies in Adriatic coastal areas; project ID 10252001) funded by the European Union under the V-A Interreg Italy-Croatia CBC programme. All the developments presented have been implemented in the Finite Element Model for Coastal Seas SHYFEM (<https://github.com/SHYFEM-model/shyfem>) developed at the CNR-ISMAR. The corresponding author is very grateful to Debora Bellafiore for its availability all along the implementation of the present work and to William McKiver for carefully reading the manuscript.

435



References

- Adcroft, A. and Campin, J.-M.: Rescaled height coordinates for accurate representation of free-surface flows in ocean circulation models, *Ocean Modelling*, 7, 269–284, 2004.
- Audusse, E., Bristeau, M.-O., Pelanti, M., and Sainte-Marie, J.: Approximation of the hydrostatic Navier-Stokes system for density stratified flows by a multilayer model: Kinetic interpretation and numerical solution, *J. Comput. Phys.*, 230, 3453–3478, 2011a.
- Audusse, E., Bristeau, M.-O., Perthame, B., and Sainte-Marie, J.: A multilayer Saint-Venant system with mass exchanges for shallow water flows. Derivation and numerical validation, *ESAIM: Mathematical Modelling and Numerical Analysis*, 45, 169–200, 2011b.
- Backhaus, J. O.: A semi-implicit scheme for the shallow water equations for application to shelf sea modelling, *Continental Shelf Research*, 2, 243–254, 1983.
- Backhaus, J. O.: A three-dimensional model for the simulation of shelf sea dynamics., *Dt. Hydrogr. Z.*, 38, 165–187, 1985.
- Bonaventura, L., Fernandez-Nieto, E. D., Garres-Diaz, J., and Narbona-Reina, G.: Multilayer shallow water models with locally variable number of layers and semi-implicit time discretization, *J. Comput. Phys.*, 364, 209–234, 2018.
- Burchard, H., Bolding, K., and Villareal, M. R.: GOTM, a General Ocean Turbulence Model. Theory, implementation and test cases, Tech. rep.
- Burchard, H. and Baumert, H.: The formation of estuarine turbidity maxima due to density effects in the salt wedge. A hydrodynamic process study, *J. Phys. Oceanogr.*, 28, 309–321, 1998.
- Burchard, H. and Petersen, O.: Hybridization between sigma- and z-coordinates for improving the internal pressure gradient calculation in marine models with steep bottom slopes, *Int. J. Numer. Meth. Fl.*, 25, 1003–1023, 1997.
- Casulli, V. and Cheng, R.: Semi-implicit finite difference methods for three-dimensional shallow water flow, *Int. J. Numer. Meth. Fluids*, 15, 629–648, 1992.
- Cheng, R., Casulli, V., and Gartner, J. W.: Tidal, Residual, Intertidal Mudflat (TRIM) model and its applications to San Francisco Bay, California., *Estuar., Coast. Shelf S.*, 36, 235–280, 1993.
- Griffies, S., Pacanowski, R., Schmidt, M., and Balaji, V.: Tracer conservation with an explicit free-surface method for z-coordinate ocean models, *Mon. Wea. Rev.*, 129, 1081–1098, 2001.
- Guardone, A., Isola, D., and Quaranta, G.: Arbitrary lagrangian eulerian formulation for two-dimensional flows using dynamic meshes with edge swapping, *J. Comput. Phys.*, 230, 7706–7722, 2011.
- Hirt, C., Amsden, A. A., and Cook, J. L.: An arbitrary Lagrangian-Eulerian computing method for all flow speeds, *J. Comput. Phys.*, 14, 227–253, 1974.
- Hordoir, R., Axell, L., Loptien, U., Dietze, H., and Kuznetsov, I.: Influence of sea level rise on the dynamics of salt inflows in the Baltic Sea., *Journal of Geophysical Research: Oceans*, 120, 6653–6668, 2015.
- Kleptsova, O., Stelling, G., and Pietrzak, D.: An accurate momentum advection scheme for a z-level coordinate models, *Ocean Dynamics*, 60, 1447–1461, 2010.
- Klingbeil, K., Lemarié, F., Debreu, L., and Burchard, H.: The numerics of hydrostatic structured-grid coastal ocean models: state of the art and future perspectives, *Ocean Model.*, 125, 80–105, 2018.
- Kuzmin, D. and Turek, S.: Flux correction tools for finite elements, *J. Comput. Phys.*, 175, 525–558, 2002.
- LeVeque, R. J.: *Finite Volume Methods for Hyperbolic Problems*, Cambridge University Press, 2002.



- Mellor, G., Hakkinen, S., Ezer, T., and Patchen, R.: A generalization of a sigma coordinate ocean model and an intercomparison of model
475 vertical grids, in: *Ocean Forecasting: Conceptual Basis and Applications*, edited by Pinardi, N. and Woods, J., pp. 55–72, Springer, New York, 2002.
- Nishikawa, H.: A truncation error analysis of third-order MUSCL scheme for nonlinear conservation laws, *Int J Numer Meth Fluids*, 93, 1031–1052, 2020.
- Oey, L.-Y.: A wetting and drying scheme for POM, *Ocean Model.*, 2, 133–150, 2005.
- 480 Song, Y. T.: A general pressure gradient formulation for ocean models: scheme design and diagnostic analysis, *Mon. Weather Rev.*, 126, 3213–3230, 1998.
- Umgiesser, G.: *SHYFEM Finite Element Model for Coastal Seas - User Manual*, Tech. rep., Oceanography, ISMAR-CNR Arsenale Tesa 104, Castello 2737/F 30122 Venezia, Italy, 2022.
- Umgiesser, G., Canu, D. M., Cucco, A., and Solidoro, C.: A finite element model for the Venice Lagoon. Development, set up, calibration
485 and validation, *Journal of Marine Systems*, 51, 123–145, 2004.
- Warner, J., Defne, Z., Haas, K., and Arango, H.: A wetting and drying scheme for ROMS, *Computers and Geosciences*, 58, 54–61, 2013.